

# Geometry and Motion Characteristics of Bubbles Released in Liquid Cross Flow

C. Kang<sup>†</sup>, W. Zhang, Y. G. Ji and Y. Cui

*School of Energy and Power Engineering, Jiangsu University, Zhenjiang, 212013, China*

<sup>†</sup>Corresponding Author Email: [kangcan@mail.ujs.edu.cn](mailto:kangcan@mail.ujs.edu.cn)

(Received May 5, 2018; accepted October 3, 2018)

## ABSTRACT

To investigate the characteristics of the bubbles trapped in liquid cross flow, air was injected into flowing water circulated in a closed loop. High speed photography was used to record bubble images instantaneously. An image-processing code was specifically developed to identify bubbles in the images and to calculate bubble parameters. Effects of the water velocity and the flow rate of the injected air on bubble patterns were investigated. The results indicate that the inclination of bubble trajectory relative to the nozzle axis is enhanced as the water velocity rises. Meanwhile, bubble size varies inversely with the water velocity. The bubble profile tends to be rounded as the water velocity increases. Fluctuations of the bubble velocity are intensified as the water velocity decreases. As the balance between the external forces exerted on the bubble is reached, an approximately linear relationship between the velocities of the bubble and the water is manifested. For a given equivalent bubble diameter, the bubble terminal velocity is higher than that associated with quiescent water. At small Eötvös number, the consistency of the bubble aspect ratio in the liquid flow and quiescent water is revealed. The range of Eötvös number is extended considerably due to the flowing water. Values of Weber number are accumulated in a range within which high bubble aspect ratio is associated with relatively high water velocity.

**Keywords:** Bubble; Liquid cross flow; Air injection; Bubble trajectory; Bubble velocity; Bubble size.

## NOMENCLATURE

$A$	area of bubble in captured image	$u_t$	bubble terminal velocity
$a$	length of the major axis of bubble	$v_b$	transverse bubble velocity
$b$	length of the minor axis of bubble	$We$	Weber number
$d$	equivalent bubble diameter	$Y$	coordinates
$E_o$	Eötvös number	$\vec{v}$	resultant bubble velocity
$E$	bubble aspect ratio	$\vec{v}_w$	additional bubble velocity
$f$	motor frequency	$\theta$	deviation angle of bubble centroid relative to nozzle axis
$q_v$	flowrate of injected air	$\rho_l$	density of water
$s$	streamwise distance between bubble centroid and the center of nozzle outlet	$\rho_g$	density of air
$U_l$	streamwise water velocity	$\sigma$	surface tension of water
$u_b$	streamwise bubble velocity		

## 1. INTRODUCTION

The bubbly flow is a unique type of multiphase flow and has remained a focal subject in both industrial and academic circles. In practice, diverse patterns of bubbly flow have been manifested. The diversity of the bubbly flows can always be related to the interaction between bubbles and the surrounding liquid. Bubbles can be generated via injecting air into

liquid. Such a strategy has been implemented by [Navisa et al. \(2014\)](#) in hydraulic and environmental engineering to improve the content of the dissolved oxygen in water, therefore providing a friendly environment for fishes and other aquatic animals. In this context, the bubble size and the distribution density of the bubbles play an important role in the enhancement of the mass transfer between the bubble and the liquid phase.

Liquid flow imposes significant effects on the trapped bubbles. Müller-Fischer *et al.* (2008) proved in shear flows that the bubble would deform due to the velocity gradients of the liquid flow. Regarding the rotating flow, it imposes the bubble with a centrifugal force, pushing the bubble move away from the rotation center (Yamaguchi *et al.* 2004). Provided that bubbles travel in a thin pipe or duct, the wall effect would inevitably influence the bubble velocity distribution as well as bubble geometry, which was demonstrated by Balzán *et al.* (2017). Particularly, the response of the bubbles near the wall to the viscous sublayer results in distinct bubble features in terms of bubble size and bubble shape relative to bubbles located elsewhere. Taking the breakup of bubble into account, the treatment of the bubbly flow is not easy (Ravelet *et al.*, 2011). It has been reported that both measurement techniques and numerical simulation have been used in bubbly flow investigation. In comparison, measurement results such as bubble size distribution are more practical even in complex bubbly wake flows (Mao *et al.*, 2018). Numerical models for depicting bubble motion have been established but the influential factors cannot be perfectly addressed according to Yapa *et al.* (2010). As bubble shape deviates considerably from the spherical form, the forces exerted on bubble surface might not be well predicted. Subsequently, the bubble motion obtained numerically differs from the real situation (Xu *et al.*, 2015).

Regarding previous study performed by Zhang *et al.* (2014) on the bubbles generated via ventilation, the emphasis was usually placed on bubble plumes instead of individual bubbles. Hitherto, the observation of individual bubbles has been performed overwhelmingly with the quiescent liquid. Trapped in the liquid flow, a bubble, along with bubble velocity components, is schematically shown in Fig. 1. As can be seen, the motion of the bubble is determined by multiple effects, which result from the forces exerted on the bubble. Among those forces, the shear force due to the velocity difference between the bubble and the liquid is dominant, which can be identified in Liu *et al.* (2010). The bubble velocity component,  $u_b$ , depends on such a shear force. This force increases with liquid velocity. The transverse velocity,  $v_b$ , could be obtained through the formula devised by Zhang *et al.* (2013). The velocity,  $\vec{v}_w$ , arises due to the wake effects of the bubble; but it was often neglected for small bubble size. It is appreciable in Fig. 1 that the direction and magnitude of the resultant bubble velocity,  $\vec{v}$ , are influenced by not just liquid flow characteristics but also the properties of the bubble itself. Certainly, there are some energy factors related to the bubbly flows, which has been considered by Li *et al.* (2018) in conjunction of the performance of the equipment.

The purpose of the present study is to obtain bubble characteristics as the bubble travels in the liquid cross flow. A water tunnel was used to provide uniform water flow. Individual bubbles were produced in the water flow through the ventilation technique. High-speed photography was used to

capture instantaneous bubble images. An image-processing code was developed to distinguish the bubble and to collect bubble data from the bubble images. The effects of the water flow velocity and the flow rate of the injected air on the bubble were jointly considered. The variations in bubble geometry and the bubble velocity with the motion of the bubble were to be explained. Moreover, the surface tension and the buoyant force associated with the bubble are anticipated to be analyzed through non-dimensional numbers; hence, an extension with respect to the existing empirical relationship, which was constructed solely for the bubble in quiescent water, would be attained.

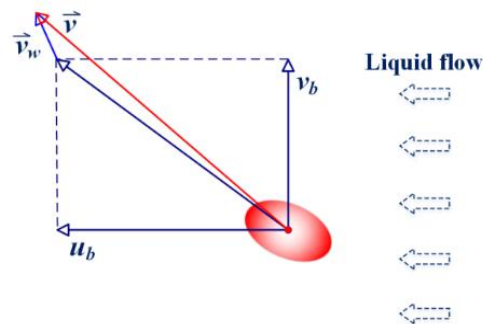


Fig. 1. Velocity components of the bubble in liquid flow.

## 2. EXPERIMENTAL SETUP

### 2.1 Closed Loop and Air-Injection Device

A closed loop suggested in Kang *et al.* (2017) was used to provide steady and uniform water flows, as shown in Fig. 2. The observation of the bubble was performed in the test section of the closed loop. The dimensions of the test section are  $0.7 \text{ m} \times 0.05 \text{ m} \times 0.315 \text{ m}$ . All the four side walls of the test section were made of plexiglass. Upstream of the test section, there is a flow stabilization segment. The magnitude of the water velocity in the test section was controlled through adjusting the frequency of the motor that drove the pump. During the circulation, the bubbles produced in the test section would collapse in the tank due to the grid plate deployed in the tank. Therefore, the flow participating in the next circulation contains pure water exclusively.

### 2.2 Optical Instrument

Prior to the experiment, velocity distributions in the test section were measured using the particle image velocimetry (PIV) technique and the PIV system of LaVision company was used, as shown in Fig. 3. An Nd:YAG laser with the light wavelength of 532 nm was used to illuminate the water flow. A CCD camera of with an image resolution of  $2456 \times 2058$  pixels was used. The image-capturing frequency was set to 14.5 fps. Hollow glass beads with diameters ranging from 20 to 50  $\mu\text{m}$  were used as tracing particles. Data acquisition and processing were conducted using Davis software.

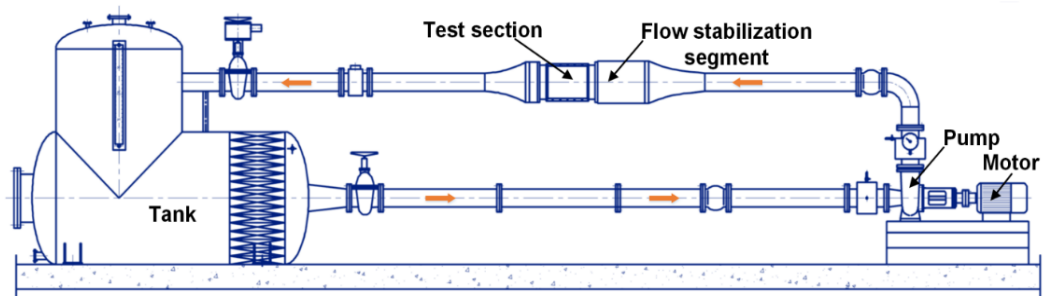


Fig. 2. Schematic diagram of the closed loop.

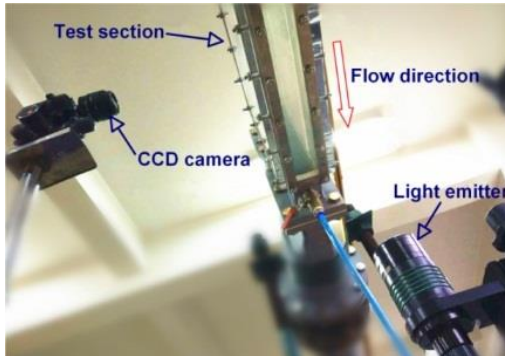


Fig. 3. Configuration of PIV components.

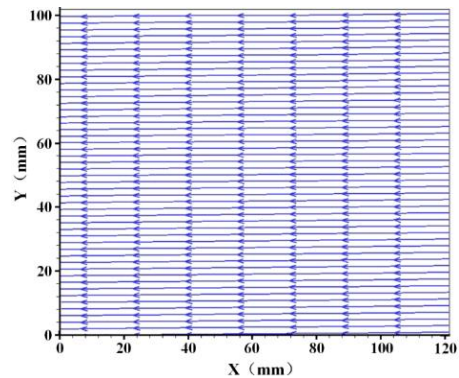
Based on averaged PIV results, streamlines over the cross section parallel to streamwise flow were obtained and are displayed in Fig. 4. The flow direction in Fig. 4 is from the right to the left; and the coordinate of  $Y=0$  mm overlaps with the horizontal symmetry centerline of the test section.

It is seen in Fig. 4 that for the two motor frequencies,  $f=7.05$  Hz and  $7.95$  Hz, water velocity distributions are uniform in both streamwise and transverse directions in the test section, furnishing a favorable environment for bubble experiments.

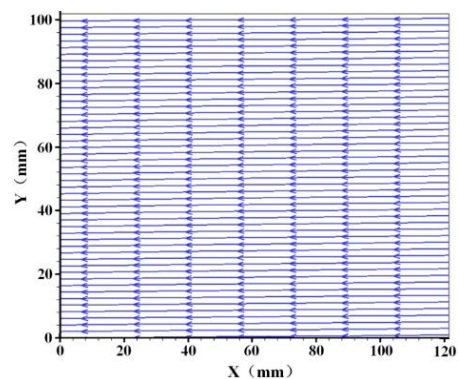
Further PIV experiments were conducted to examine the operation stability of the water tunnel. For different motor frequencies between  $f=7.05$  Hz and  $7.95$  Hz, water velocity in the test section was measured. The magnitude of the water velocity,  $U_i$ , is plotted as a function of  $f$  in Fig. 5. The correspondence between  $U_i$  and  $f$  is remarkable. Moreover, the data points displayed in Fig. 5 can be well fitted with a linear relationship, which is formulated in Fig. 5 as well. Therefore, stable operation of the water tunnel was proven; furthermore, the comparison of bubble properties for different water flow velocities would be reasonable. Turbulent fluctuations in the test section was reduced via the stabilization segment deployed upstream of the test section. In this context, the influence of turbulent fluctuations on the bubble described in [Martínez-bazán \*et al.\* \(1999\)](#) is beyond the scope of the present study.

A circular brass tube, with an inner diameter of  $3.0$  mm and out diameter of  $5.0$  mm, served as a nozzle and was installed in the test section for discharging air into the water tunnel. The axis of the nozzle was vertical to the water flow direction

and the nozzle outlet was positioned at  $Y=0$  mm. A syringe pump was used to drive the injection of air into the water flow. The flow rate of the injected air,  $q_v$ , was adjustable. The configuration of the ventilation components is shown in Fig. 6. [Baylar \*et al.\* \(2010\)](#) proved that the air-injection manner has a remarkable effect on bubble geometry and the bubble distribution density. The air-injection approach adopted here ensured that bubbles were released in the same plane. Meanwhile, with the cooperation between the flow rate of the injected air and the water flow velocity, the overlapping between bubbles was avoided. In comparison, bubble plumes have been reported in a ventilation study performed by [Wei \*et al.\* \(2015\)](#). In that case, the bubble-bubble interaction cannot be neglected; and bubbly flow patterns can be recognized merely from an overall view.



(a)  $f=7.05$  Hz



(b)  $f=7.95$  Hz

Fig. 4 Streamline patterns in the test section.

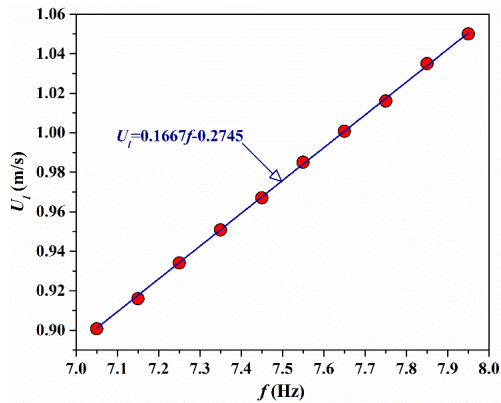


**Fig. 5. Variation of water velocity magnitude with the motor frequency.**

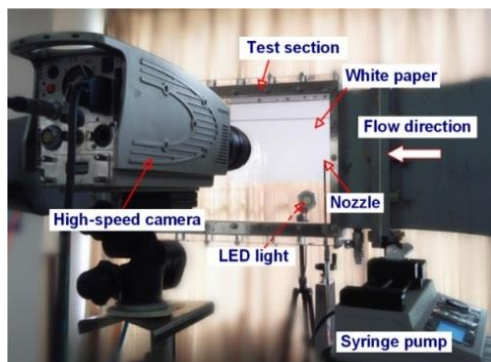


**Fig. 6. In-situ image of high-speed photography experiment.**

Bubble images were recorded using an OLYMPUS I-SPEED 3 high-speed camera in conjunction with an OLYMPUS ILP-2 light source, as shown in Fig. 6. The depth of view (DOV) plane was set to overlap with the plane passing through the axis of the nozzle. The light passes through a white paper before penetrating into the water flow. The paper was used to uniformize the incident light onto the DOV plane; thereby, the monitored window was dominated by identical light intensity. Considering the magnitude of the bubble velocity, the exposure time and the frame rate of the camera were set as 0.5 ms and 3000 fps, respectively. The size of the monitored window was determined jointly by expected resolutions of captured images, the camera lens and the relative distance between the lens and the DOV plane.

### 2.3 Bubble Image Processing Code

To extract quantitative bubble information from the bubble images captured, an image-processing code was developed based on the commercial MATLAB software. The major steps incorporated in the code are displayed in Fig. 7. Regarding available commercial code packages affiliated to high-speed cameras or multiphase flow measurement

instruments, the parameter setting involved is difficult to fully understand. As these code packages are used to treat different bubble patterns, it is not an easy task to evaluate the accuracy of the obtained results. Therefore, an in-house code for processing bubble images was specifically developed to deal with the bubble images captured here.

In the captured images, the gray scale values associated with the bubble were different from the remaining parts, which opened the possibility of isolating the bubble in the image. The primary function of the developed code in the present study is to identify the bubble and to calculate the geometric parameters and the velocity of the bubble. The background image, which was captured at the same position but without the participation of the bubble, was subtracted from the raw bubble image. The contrast in the image was improved through an image binarisation algorithm. Then the median filter algorithm was used to smooth the image. As one of the most important procedures, the edge of the bubble was traced and extracted using the Canny algorithm (Ding and Goshtasby, 2001). A linear smoothing filter was used for reducing noise for the extracted bubble edge. After the processing of consecutively captured bubble images for the same monitored window, instantaneous bubble edges were obtained and arranged sequentially in one single diagram. Therefore, the trajectory of the bubble was obtained.

Based on the observation, most bubbles had an ellipsoidal shape. Therefore, in the code developed, the length of the major axis,  $a$ , the length of the minor axis,  $b$ , and the centroid position of the bubble were calculated for each bubble. Then the correspondence between pixels in the image and the physical dimensions was established using the image of a ruler. Consequently, the area covered by the bubble,  $A$ , the equivalent bubble diameter,  $d$ ,  $d=(4A/\pi)^{0.5}$ , and the aspect ratio,  $E$ ,  $E=b/a$ , were obtained. For the same bubble in two neighboring images, the bubble displacement was calculated according to the relative position of one centroid with respect to the other; hence, the bubble velocity was calculated in consideration of the predefined time interval.

## 3. RESULTS AND DISCUSSION

### 3.1 Bubble Trajectory

For three flow rates of injected air, namely 400, 700 and 1000 ml/h, and three water velocities, namely 0.90, 0.97 and 1.03 m/s, the bubble trajectories obtained are plotted in Fig. 8. It is worthwhile to note that with the combinations of the two operation parameters considered here, the time intervals between the generation of two neighboring bubbles are sufficiently long; therefore, the interaction between the neighboring bubbles was neglected.

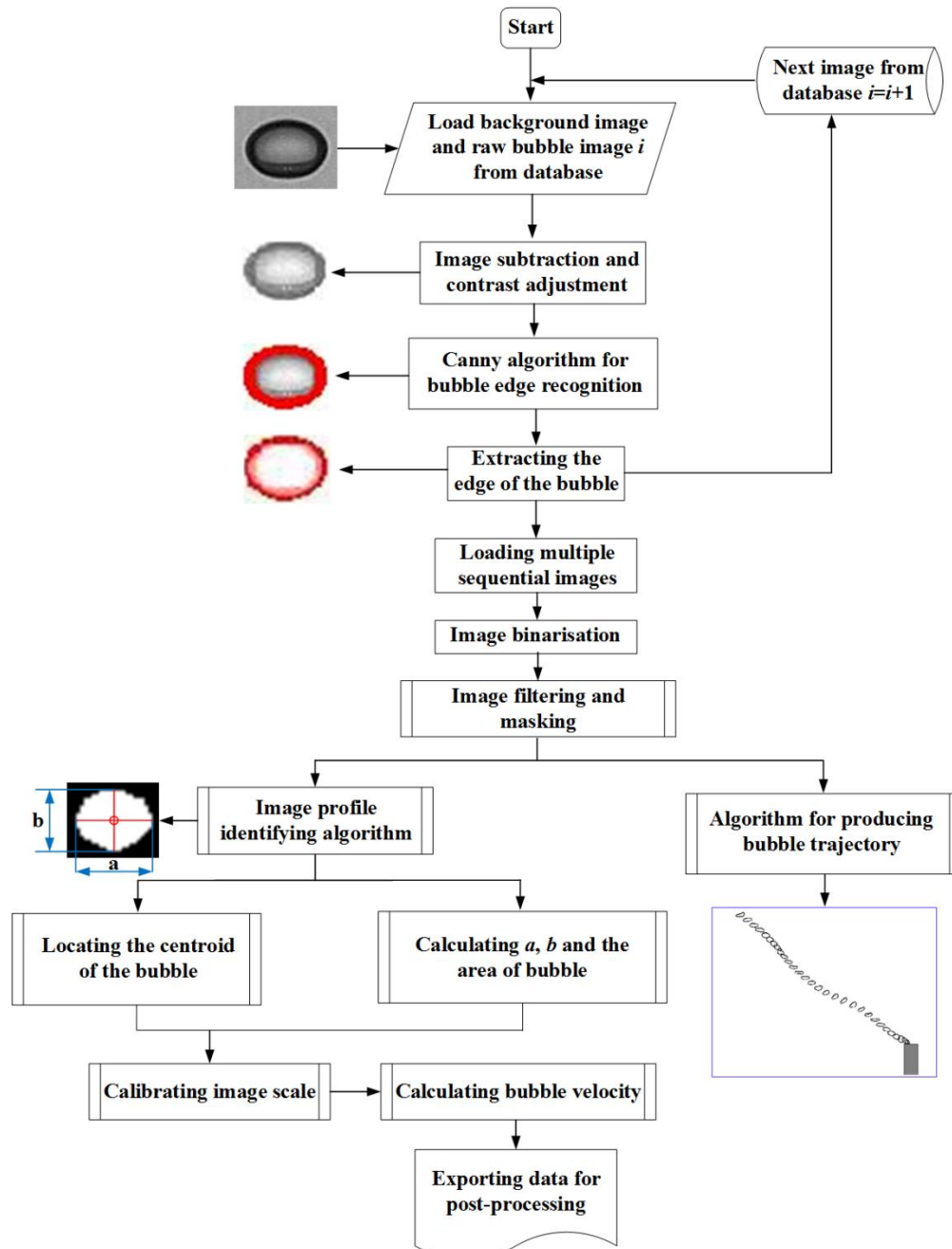


Fig. 7. Framework of the bubble image processing code.

Each subfigure is composed of successive profiles of the same bubble at different moments. As can be seen, for  $U_l=0.90$  m/s, bubble size is fairly large; moreover, bubbles are featured by flat ellipsoidal shapes. With the increase in the water velocity, the bubble size decreases continuously; meanwhile, bubbles tend to be rounded. For  $U_l=1.03$  m/s, the bubble trajectory deviates remarkably from the vertical direction. In contrast, at  $U_l=0.90$  m/s, the inclination of the bubble trajectory towards the water flow direction is relatively alleviated; however, the distortion of the bubble trajectory is perceivable, which is particular obvious at  $q_v=400$  ml/h. In comparison, for  $U_l=0.97$  m/s and 1.03 m/s, the bubble trajectory is less sensitive to the variation in  $q_v$ , as demonstrated in Fig. 8.

It was reported in Liu *et al.* (2015) that the trajectory of the rising bubble in quiescent liquid incorporated two segments, namely an initial linear segment and then a sinusoidal segment. As can be seen in Fig. 8, the situation at  $U_l=0.90$  m/s and  $q_v=400$  ml/h is rather similar to that in quiescent liquid. Moreover, it was revealed by Jobehdar *et al.* (2013) that the vertical rising of the bubble can maintain for a long distance for low water velocities. In the present study, with the increase in the air flow rate, the initial vertical trajectory segment is apparently shortened. As the water velocity increases, even the trajectory oscillation at the latter stage is attenuated and the bubble trajectory is apparently straightened. As the water velocity increases further, the drag force from the flowing water turns to be remarkable. It is

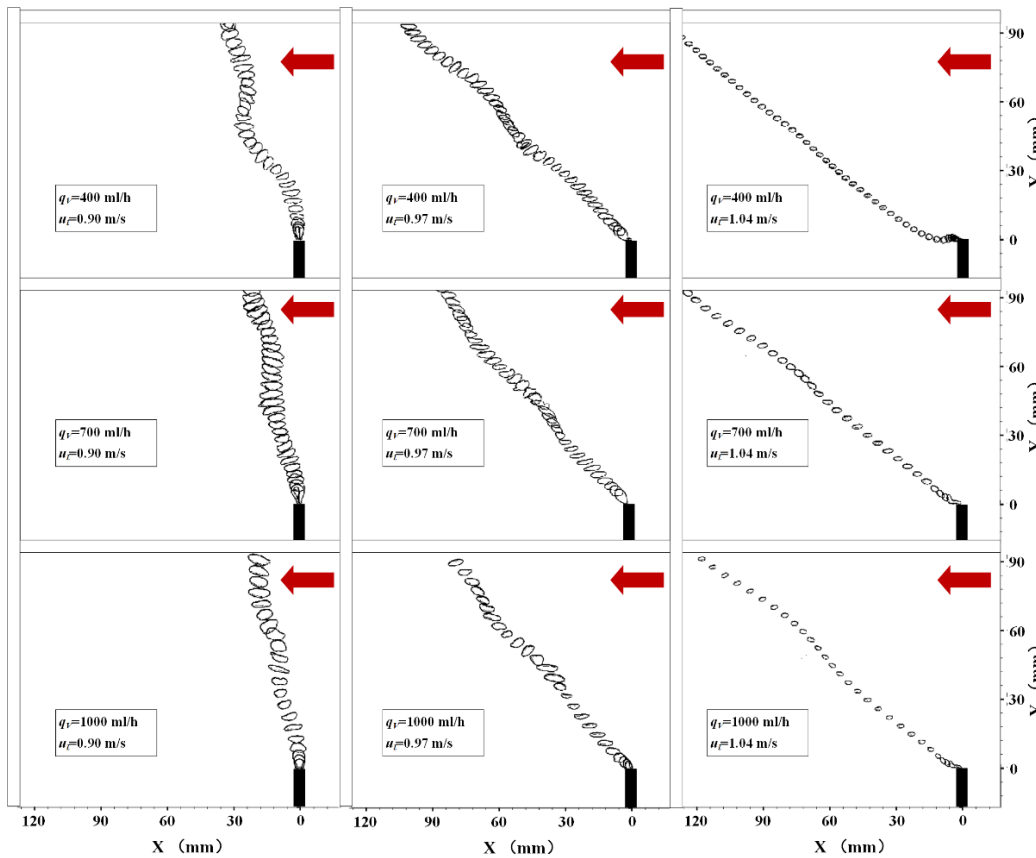


Fig. 8. Variation of bubble trajectory pattern with air flow rate and water velocity.

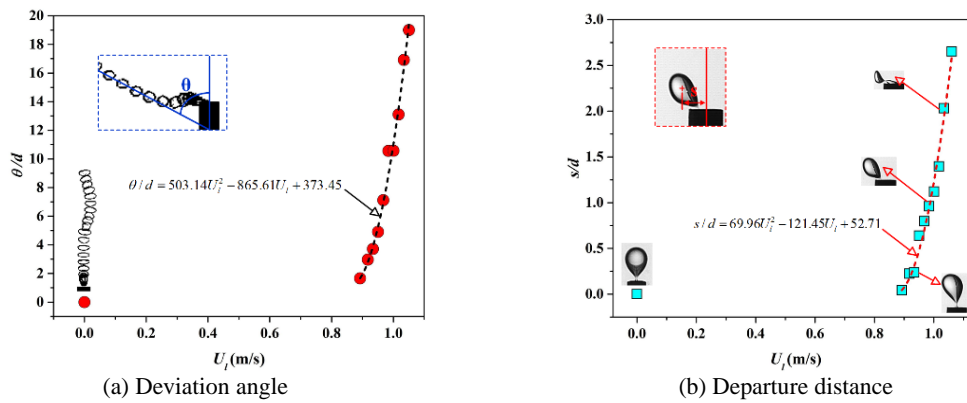


Fig. 9. Variation of bubble trajectory parameters with water velocity for  $q_v=400$  ml/h.

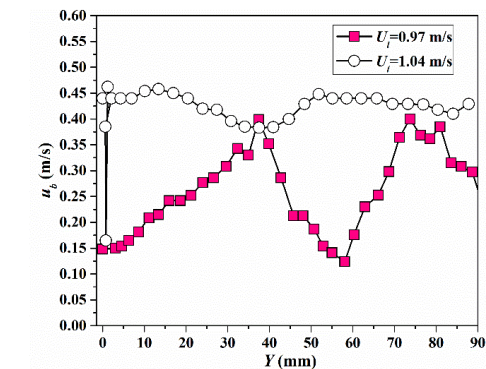
perceivable the integrity of large bubbles will be impaired. Meanwhile, it is possible that bubbles will be involved in the wake region downstream of the nozzle.

The evolution of the bubble at the initial stage was evidently related to the water velocity. Therefore, two parameters, namely the deviation angle,  $\theta$ , and the departure distance,  $s$ , were defined to further explain the deformation of the bubble trajectory near the nozzle, as illustrated in Fig. 9. For  $q_v=400$  ml/h, the variations in  $\theta$  and  $s$ , which were non-dimensionalized with the equivalent bubble diameter,  $d$ , as the function of the water velocity are plotted in Figs. 9(a) and (b), respectively. As can be

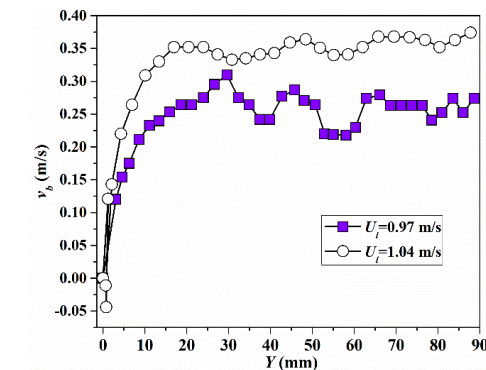
seen in Fig. 9(a), for  $U_l < 0.90$  m/s, the increase in  $U_l$  only leads to a slight increase in the deviation angle. While for  $U_l > 0.90$  m/s, the deviation angle increases sharply with the increase in the water velocity; furthermore, the data points can be approximated with a quadratic relationship, as demonstrated in Fig. 9(a) as well. In this context, it should be pointed out that the bubble trajectory is influenced by not just the water velocity but also the equivalent bubble diameter.

The relationship between  $s$  and  $U_l$  is similar to that indicated in Fig. 9(a). In the same fashion, a quadratic relationship was constructed to cover the data points at  $U_l > 0.90$  m/s. The increase in  $U_l$  results

in a synchronous increase in the shear force exerted on the bubble surface, which is produced due to the velocity difference between the water and the bubble. In this case, the vertical rising of the bubble is subjected to a large resistance. Moreover, it is seen that at high water velocity, large bubble cannot take into shape at the nozzle outlet; alternatively, a small bubble is created as a response to the horizontal disturbance by the water flow. Similar results of bubble deformation have been reported in the work of [Katoh \*et al.\* \(2011\)](#) on the evolution of the bubble in the turbulent boundary layer. It is conjectured that as the water velocity increases further, bubble rising will be replaced with horizontal or downward bubble motion and bubbles will be involved in the wake flow downstream of the nozzle.



(a) Horizontal velocity component



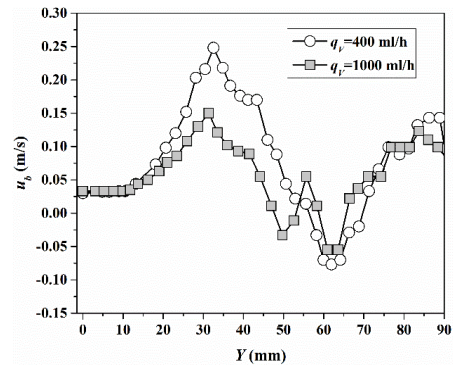
(b) Vertical velocity component

**Fig. 10. Variations of bubble velocity at different water flow velocities.**

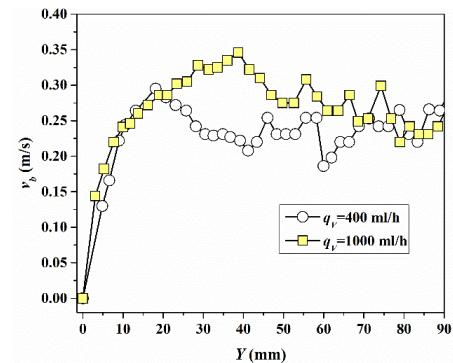
### 3.2 Bubble Velocity Components

For  $q_v=400$  ml/h, the variations in the bubble velocity components, namely  $u_b$  and  $v_b$ , as a function of the vertical distance from the nozzle outlet are plotted in Figs. 10(a) and (b), respectively. The data presented here were examined and approved in different sample groups. As can be seen, higher water velocity is associated with higher bubble velocity, as is shared by both  $u_b$  and  $v_b$ . In Fig. 10(a), for  $U_i=1.04$  m/s,  $u_b$  manifests an abrupt fluctuation as the bubble detaches from the nozzle, as occurs as well in Fig. 10(b). In this case, the bubble bounds back as it separates entirely from the nozzle. For  $U_i=0.90$  m/s, the negative values of  $v_b$  arise, which is

caused by the strong downward suppression of the bubble rising by the water flow. In Fig. 10(b), for  $U_i=0.97$  m/s, the vertical bubble velocity,  $v_b$ , increases sharply to its maximum value and then fluctuates around 0.25 m/s. The increase in the water velocity leads to the attenuation of the fluctuation of  $v_b$ . In comparison, the discrepancy in horizontal bubble velocity,  $u_b$ , between the two cases is remarkable. Low water flow velocity is featured by drastic fluctuations of  $u_b$ . Regarding the situation in quiescent water, it has been concluded by [Ellingsen and Risso \(2001\)](#) that the wake vortices generated behind the bubble have a strong influence on the bubble velocity. In the present study, the wake effect is anticipated as well; but such an effect is more evident at the lower water velocity. With the increase in the water velocity, the streamwise impetus behind the bubble motion exceeds the disturbance of wake vortices; therefore, variations in both the two bubble velocity components are restricted.



(a) Horizontal velocity component



(b) Vertical velocity component

**Fig. 11. Variations of bubble velocity at different air flow rates.**

For  $U_i=0.90$  m/s, the variations in  $u_b$  and  $v_b$  with the movement of the bubble are shown in Fig. 11. On the whole, the influence of the air flow rate on the two bubble velocity components is not significant. In Fig. 11(a), the low air flow rate is matched with relatively high streamwise bubble velocity, as is distinct for  $Y=20$  to  $50$  mm. Nevertheless, for the vertical velocity,  $v_b$ , the tendency is reversed. Similar conclusions have been obtained with the quiescent liquid by [Wang and Socolofsky \(2015\)](#). As  $q_v$  increases, the increase in bubble size triggers an increase in the buoyant force; therefore, the

acceleration stage of the bubble is extended, as indicated in Fig. 11(b). After a short distance which is dominated by bubble acceleration,  $v_b$  fluctuates for a vertical distance and then the bubble terminal velocity is attained at approximately  $Y=45$  mm. In this context, at any given water velocity, the bubble terminal velocity varies only slightly with the increase in the air flow rate.

It is seen in Figs. 10 and 11 that there is a large velocity gap between the streamwise bubble velocity and the water velocity. To seek the correlation between the two velocities, the streamwise bubble velocity is averaged as the bubble velocity attains the terminal velocity. The variation of the bubble terminal velocity,  $u_t$ , obtained through averaging bubble velocity within  $45 \text{ mm} < Y < 90 \text{ mm}$ , with the water velocity,  $U_t$ , is plotted in Fig. 12.

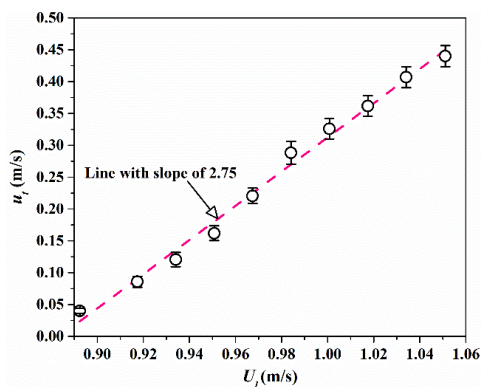


**Fig. 12. Variation of horizontal bubble terminal velocity with water velocity.**

It is evident that there is a nearly linear relationship between the bubble velocity and the water velocity. A fitting line with a slope of 2.75 is plotted in Fig. 12 as well. With the variation in the water velocity, the motion of the bubble will reach a balance state in the streamwise direction, as is determined by the impetus from the water and the resistance of the bubble to that force. Furthermore, the tendency indicated in Fig. 12 applies to all bubbles observed in the presented experiment.

### 3.3 Equivalent Bubble Diameter and Bubble Shape

The influence of the air flow rate on the bubble size has been demonstrated in [Ghaemi \*et al.\* \(2010\)](#). Here, an extension based on the previous result was attained with the influence of the water velocity being considered. The equivalent bubble diameter,  $d$ , was calculated as the water velocity,  $U_t$ , was varied from 0.90 to 1.05 m/s. For each velocity, the bubbles did not overlap with each other and individual bubbles were identifiable. The bubble terminal velocity,  $u_t$ , was obtained using the above approach. Moreover, the results based on the empirical formula proposed for the quiescent liquid in [Tomiyama \*et al.\* \(2002\)](#) are presented as well.

The effect of the water velocity on the bubble terminal velocity is significant. For  $U_t=0.90$  m/s, the horizontal disturbance on the bubble is slight and the

data points approach the results in [Tomiyama \*et al.\* \(2002\)](#). Overall, with the increase in the water velocity, the bubble terminal velocity increases and the equivalent bubble diameter decreases. The sparsely distributed data points imply a global trend that the bubble terminal velocity varies inversely with the equivalent bubble diameter. This conforms to the general knowledge of bubbly dynamics. In this context, although bubbles manifest with various size and shape, the geometric and kinematic parameters are inherently related.

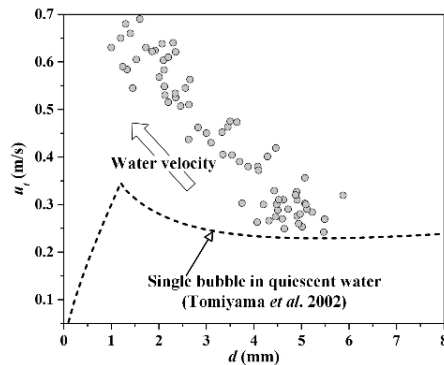


**Fig. 13. Variation of bubble terminal velocity with equivalent bubble diameter.**

Of interest is the bubble deformation in the liquid cross flow, which is described through the bubble aspect ratio,  $E$ . The correspondence between  $E$  and  $d$  is illustrated in Fig. 14. The bubble aspect ratio was calculated statistically for each water velocity. As can be seen, there is no explicit relationship between  $E$  and  $d$ . Nevertheless, three zones are roughly recognizable in Fig. 14. Zone A is associated with high water velocity. In this zone,  $E$  is high and  $d$  is less than 2.5 mm. In Zone B, the water flow velocity falls within an intermediate range. The values of  $E$  indicate that bubbles in Zone B exhibit clearly flat shape; meanwhile,  $d$  ranges from 2.5 to 4.0 mm. Regarding Zone C, relatively low water flow velocities are covered; moreover, the equivalent bubble diameter,  $d$ , exceeds 4.0 mm and  $E$  is relatively low. On the whole, the bubble aspect ratio shown in Fig. 14 is lower than 0.6, which is much lower than its counterpart associated with quiescent water ([Mikaelian \*et al.\*, 2013](#)). Therefore, the effect of the water velocity on the bubble aspect ratio is demonstrated.

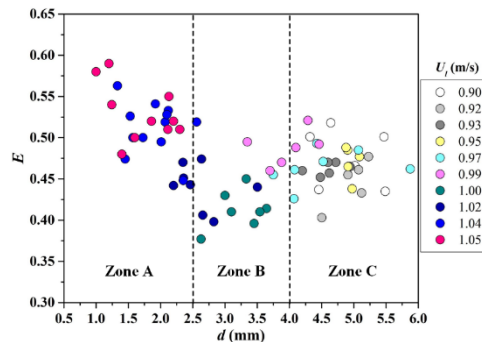


**Fig. 14. Correspondence between bubble aspect ratio and equivalent bubble diameter.**

#### 4. BUBBLE DEFORMATION AND DIMENSIONLESS NUMBERS

Regarding the bubbles involved in the liquid cross flow, both the geometric and kinetic features can be traced to the forces exerted on the bubble. Among the forces, the buoyant force and the surface tension force deserve particular consideration. The comparison of the forces has been implemented in [Dong \*et al.\* \(2010\)](#) through dimensionless numbers. In this context, the Eötvös number ( $Eo$ ) is defined as:

$$Eo = \frac{g(\rho_l - \rho_g)d^2}{\sigma} \quad (1)$$

where  $\rho_l$  and  $\rho_g$  denote water and air density, respectively;  $d$  is the equivalent bubble diameter, which serves as a characteristic length;  $\sigma$  denotes the surface tension of water.

Essentially,  $Eo$  is a ratio of the buoyant force to the surface tension force. For different water velocities, the bubble aspect ratio is plotted as a function of  $Eo$  in Fig. 15. Meanwhile, the relationship between  $E$  and  $Eo$  for quiescent water proposed in [Okawa \*et al.\* \(2003\)](#) is presented. For  $Eo < 1$ , the data points of  $E$  obtained here are distributed on both sides of the curve obtained in [Okawa \*et al.\* \(2003\)](#); in this case, the equivalent bubble diameter is less than 2.8 mm and the water velocity is relatively high. Meanwhile, for  $Eo < 1$ , the bubble aspect ratio is sensitive to the variation of  $Eo$ , as is recognizable in Fig. 15. In contrast, for  $Eo > 1$ , with the increase in  $Eo$ , the bubble aspect ratio fluctuates roughly between 0.4 and 0.6. It should be noted that the  $Eo$  values obtained here exceed those associated with quiescent liquid. On the whole, with the increase in  $U_i$ ,  $Eo$  decreases, which implies that the influence of the buoyant force on the bubble decays rapidly relative to that of the surface tension force.

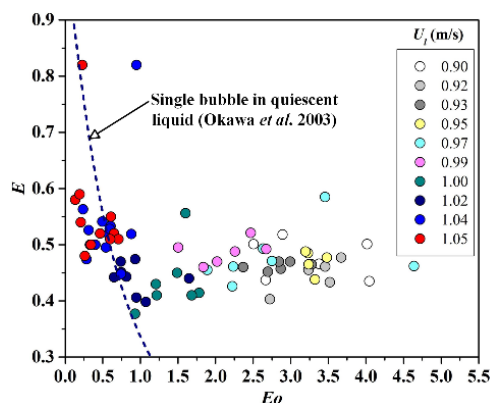


Fig. 15. Variation of bubble aspect ratio with  $Eo$  for different water velocities.

Weber number ( $We$ ) is another dimensionless number and is defined as the ratio of the inertial force to the surface tension force. In the present study,  $We$  is given by:

$$We = \frac{\rho_l u_i d}{\sigma} \quad (2)$$

Here, the bubble terminal velocity was used in the definition of  $We$  in the liquid flow. The variation of the bubble aspect ratio with Weber number at different upstream flow velocities is illustrated in Fig. 16. Meanwhile, the relationship associated with the single isolated bubble in quiescent water is plotted as well.

It is seen that the experimental data are located in the range of  $3.8 < We < 13$  and nearly symmetrically distributed on both sides of the curve corresponding to the single bubble in quiescent water. A global view shows that high water velocity is generally responsible for high bubble aspect ratio. Although  $We$  is proportional to the bubble terminal velocity, as indicated in Eq. (2), there is no explicit relationship between  $We$  and the water velocity. The contribution of the equivalent bubble diameter is significant. The equivalent bubble diameter decreases and the bubble aspect ratio rises overall with the decline of  $We$ . Nevertheless, the shrinking of the bubble would in turn lower the surface tension force and  $We$  tends to be enlarged. There is an equilibrium between the drag force and the surface tension force; therefore, the  $We$  values for the bubble in the liquid cross flow are accumulated within a certain range.

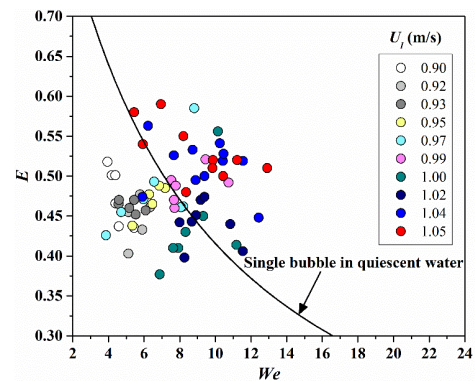


Fig. 16. Variation of bubble aspect ratio with  $We$  for different water velocities.

#### 5. CONCLUSIONS

(1) As the water flow velocity increases, the deviation of the bubble trajectory relative to the air injection direction becomes remarkable; meanwhile, bubble size decreases and bubble shape shifts from flat ellipsoidal shape to rounded shape. For a given water flow velocity, the variation in the air flow rate causes a slight change in bubble geometry.

(2) The traveling bubble in water flow experiences velocity fluctuations. Velocity fluctuations in both the water flow direction and the air injection direction are intensified as the water velocity decreases. As the balance state for the bubble is attained, there is an approximately linear relationship between the bubble velocity and the water flow velocity.

(3) The bubble aspect ratio for small Eötvös number agrees with that in quiescent water; however, large Eötvös number obtained here is beyond the scope obtained in the quiescent water, and corresponding

bubble aspect ratio is low. Values of Weber number are accumulated in a narrow range relative to those associated with bubbles rising in quiescent water.

#### ACKNOWLEDGEMENTS

The authors are grateful to the financial support provided by National Natural Science Foundation project under Grant No. 51676087. The authors also appreciate those suggestions from the technicians of Cinv Optical Instruments Co., LTD in assessing the bubble visualization experiment uncertainty.

#### REFERENCES

- Balzán, M. A., R. S. Sanders and B. A. Fleck (2017). Bubble formation regimes during gas injection into a liquid cross flow in a conduit. *The Canadian Journal of Chemical Engineering* 95, 372–385.
- Baylar, A., F. Ozkan and M. Unsal (2010). Effect of air inlet hole diameter of venturi tube on air injection rate. *KSCE Journal of Civil Engineering* 14, 489–492.
- Ding, L. and A. Goshtasby (2001). On the Canny edge detector. *Pattern Recognition* 34, 721–725.
- Dong, H., X. Wang, L. Liu, X. Zhang and S. Zhang (2010). The rise and deformation of a single bubble in ionic liquids. *Chemical Engineering Science* 65, 3240–3248.
- Ellingsen, K. and F. Risso (2001). On the rise of an ellipsoidal bubble in water: oscillatory paths and liquid-induced velocity. *Journal of Fluid Mechanics* 440, 235–268.
- Ghaemi, S., P. Rahimi and D. S. Nobes (2010). The effect of gas-injector location on bubble formation in liquid cross flow. *Physics of Fluids* 22, 043305.
- Jobehdar, M. H., A. H. Gadallah, K. Siddiqui and W. A. Chishti (2013). Investigation of the bubble formation in liquid cross-flow using a novel nozzle design. In *Proceedings of the ASME 2013 Fluids Engineering Division Summer Meeting*, Nevada, USA.
- Kang, C., W. Zhang, Y. Gu and N. Mao (2017). Bubble size and flow characteristics of bubbly flow downstream of a ventilated cylinder. *Chemical Engineering Research and Design* 122, 263–272.
- Katoh, K., Y. Arii and T. Wakimoto (2011). Bubble formation from an air jet injected into a turbulent boundary layer. *Journal of Fluid Science and Technology* 6(4), 528–541.
- Li, X., Z. Jiang, Z. Zhu, Q. Si and Y. Li (2018). Entropy generation analysis for the cavitating head-drop characteristic of a centrifugal pump. *Proceedings of the Institution of Mechanical Engineers Part C Journal of Mechanical Engineering Science*.
- Liu, C., B. Liang, S. Tang, H. Zhang and Z. Min (2010). A theoretical model for the size prediction of single bubbles formed under liquid cross-flow. *Chinese Journal of Chemical Engineering* 18, 770–776.
- Liu, L., H. Yan and G. Zhao (2015). Experimental studies on the shape and motion of air bubbles in viscous liquids. *Experimental Thermal Fluid Science* 62, 109–121.
- Mao, N., C. Kang, W. Opare and Y. Zhu (2018). Hydrodynamics features of dispersed bubbles in the ventilated wake flow of a cylinder. *Chinese Journal of Chemical Engineering* 26, 1803–1813.
- Martínez-bazán, C., J. L. Montañés and J. C. Lasheras (1999). On the breakup of an air bubble injected into a fully developed turbulent flow. Part 1. Breakup frequency. *Journal of Fluid Mechanics* 401, 157–182.
- Mikaelian, D., A. Larcy, S. Dehaeck and B. Haut (2013). A new experimental method to analyze the dynamics and the morphology of bubbles in liquids: Application to single ellipsoidal bubbles. *Chemical Engineering Science* 100, 529–538.
- Müller-Fischer, N., P. Tobler, M. Dressler, P. Fischer and E. J. Windhab (2008). Single bubble deformation and breakup in simple shear flow. *Experiments in Fluids* 45, 917–926.
- Navisa, J., T. Sravya, M. Swetha and M. Venkatesan (2014). Effect of bubble size on aeration process. *Asian Journal of Scientific Research* 7(4), 482–487.
- Okawa, T., T. Tanaka and I. Kataoka (2003). Temperature effect on single bubble rise characteristics in stagnant distilled water. *International Journal of Heat and Mass Transfer* 46, 903–913.
- Ravelet, F., C. Colin and F. Risso (2011). On the dynamics and breakup of a bubble rising in a turbulent flow. *Physics of Fluids* 23, 103301.
- Tomiyama, A., G. P. Celata, S. Hosokawa and S. Yoshida (2002). Terminal velocity of single bubbles in surface tension force dominant regime. *International Journal of Multiphase Flow* 28, 1497–1519.
- Wang, B. and S. A. Socolofsky (2015). On the bubble rise velocity of a continually released bubble chain in still water and with crossflow. *Physics of Fluids* 27, 103301.
- Wei, W., J. Deng, F. Zhang and Z. Tian (2015). A numerical model for air concentration distribution in self-aerated open channel flows. *Journal of Hydrodynamics* 27, 394–402.
- Xu, Y., M. Ersson and P. G. Jönsson (2015). A mathematical modeling study of bubble formations in a molten steel bath. *Metallurgical and Materials Transactions B* 46B, 2628–2638.

- Yamaguchi, T., M. Iguchi and T. Uemura (2004). Behavior of a small single bubble rising in a rotating flow field. *Experimental Mechanics* 44, 533–540.
- Yapa, P.D., L. K. Dasanayaka, U.C. Bandara and K. Nakata (2010). A model to simulate the transport and fate of gas and hydrates released in deepwater. *Journal of Hydraulic Research* 48(5), 559–572.
- Zhang, W. and Z. Z. David (2013). Bubble characteristics of air–water bubbly jets in crossflow. *International Journal of Multiphase Flow* 55, 156–171.
- Zhang, W. and Z. Z. David (2014). Trajectories of air-water bubbly jets in crossflows. *Journal of Hydraulic Engineering* 140, 06014011.